Advances in Science and Technology Research Journal

Advances in Science and Technology Research Journal, 2026, 20(10), 266–281
https://doi.org/10.12913/22998624/225588
ISSN 2299-8624, License CC-BY 4.0

Received: 2026.04.22
Accepted: 2026.07.07
Published: 2026.09.01

Non-isothermal computational fluid dynamics analysis of electrically assisted heating system for faster catalyst activation

Roger Taipe Suni[1], John Alejandro Yana Gutierrez[1], Yuri Lester Silva Vidal[1], Diego Fernando Macedo Calcina[1], Christofer Alex Diaz Arapa[1*]

[1] Universidad Nacional de San Agustín de Arequipa, Arequipa 04000, Perú
* Corresponding author's e-mail: cdiazar@unsa.edu.pe

ABSTRACT

Cold start in internal combustion engines represents a critical phase in emissions control, because the catalytic converter has not yet reached its activation temperature (light-off), resulting in elevated emissions of carbon monoxide (CO), unburned hydrocarbons (HC), and nitrogen oxides (NO_x). In this study, a non-isothermal 3D CFD Model is developed to evaluate a novel Active Hybrid Thermal Strategy for a three-way catalytic converter. The proposed strategy introduces a dual-stage heating approach that combines external and internal heat generation with the objective of reducing light-off time, achieving a uniform temperature distribution and reducing the emission of NO_x. The proposed approach was benchmarked against several heating configurations to demonstrate its improved thermal performance. The results show that electrical heating significantly reduces the light-off time by 71.3% compared to the baseline. Under cold-start conditions, the hybrid system limits NO_x emissions to 47.47 mg/km, meeting the Euro 7 regulatory limit of 60 mg/km. These findings confirm that hybrid EHC technology is a promising alternative for meeting stringent upcoming emission regulations. These results demonstrate the potential of hybrid electrically assisted heating strategies to improve catalytic converter performance during cold-start operation.

Keywords: catalytic converter, electric heating, computational fluid dynamics, light-off, automotive sustainability.

INTRODUCTION

Automotive transportation based on internal combustion engines continues to be one of the fundamental pillars of modern mobility. The emissions generated by these engines include compounds such as carbon monoxide (CO), unburned hydrocarbons (HC), and nitrogen oxides (NO_x), which are harmful to the environment and contribute to the deterioration of air quality [1, 2].

These emissions increase during cold start. During this initial phase, the catalytic converter (responsible for chemically transforming harmful exhaust gases into less harmful compounds) has not yet reached its activation temperature, known as the light-off temperature, which is typically around 250 °C [3]. In this state, the oxidation and reduction reactions occurring on the catalytic surface are inefficient or even nonexistent, causing a significant fraction of the pollutants emitted by the engine to be released directly into the atmosphere. The time required for the catalyst to reach its light-off temperature may vary depending on ambient temperature, engine type, catalyst mass, and exhaust system configuration [4].

The origin of this problem lies in the high thermal inertia and low thermal conductivity of the catalyst, which delays its heating and leads to non-uniform temperature distributions during the initial stages of operation [5]. In addition, the catalytic monolith presents thermal limitations, since temperatures above 1000 °C may compromise its structural integrity and catalytic performance [6, 7].

In recent years, one of the most promising alternatives to reduce light-off time has been the electrical heating of the catalyst. This technique employs electrically heated metallic monoliths (EHC) [8, 9]. However, their effectiveness as the sole element for filtering harmful exhaust gases may be limited, and these systems present challenges related to thermal distribution, energy consumption, and integration with the exhaust system [6, 10].

In this context, the present study evaluates, through computational fluid dynamics (CFD) using ANSYS Fluent, a novel Active Hybrid Thermal Strategy that combines external heating resistances with an electrically heated catalyst (EHC). The analysis focuses on the thermo-fluid interaction between the exhaust gases and the ceramic monolith during cold start, considering different electrical heating strategies.

The evaluation focuses on the time required to reach the light-off regime, the uniformity of the thermal distribution within the monolith and peak temperatures. Furthermore, this study transcends purely thermal analysis by implementing an Integrated Multi-Physical script, which quantifies cumulative mass emissions and benchmarking them against the Euro 7 standard limits. In this way, the study aims to establish a technical basis for the design and optimization of electrical heating strategies that reduce thermal peaks and accelerate catalyst activation, thereby contributing to the reduction of pollutant emissions under cold-start conditions [11, 12]. Furthermore, the present study incorporates numerical verification and qualitative benchmarking against previously reported catalytic converter CFD studies to ensure consistency of the predicted thermal and light-off behavior.

METHODOLOGY

The present research is conducted using a CFD approach with ANSYS Fluent, with the objective of reducing light-off time and achieving a uniform temperature distribution in the ceramic monolith [13]. This methodology begins with the characterization of the monolith as an equivalent porous medium [14, 15], followed by the simulation of the complete system (catalytic converter and primary exhaust pipe), considering square and hexagonal cell geometries for the ceramic monoliths. Based on this comparison, the most efficient configuration is selected, on which different electrical heating strategies are evaluated, including an EHC and band-type heating resistances, whose geometry is defined by a metallic casing that encapsulates a helical resistive element.

Once the best technique is selected, through the Arrhenius equation, mass flux conservation, and flow reactor equations, the NOx, CO, and HC emissions are evaluated [13, 14].

Design and material definition

At this stage, three-dimensional modeling of the complete system, shown in Figure 1, was carried out using Autodesk Inventor. In addition, two representative geometric configurations of the catalytic monolith were developed: square-section cells and hexagonal-section cells. The dimensions and geometric configurations are based on values reported for automotive catalytic converters used in light commercial vehicles, such as the Toyota Hilux [16, 17]. Furthermore, the sizing and material properties of the heating resistors were integrated into the model using technical data extracted from specialized component distributors [18, 19], ensuring that the heater's geometry and thermal response are consistent with commercially available technology.

For numerical analysis, the geometry was prepared in ANSYS Space Claim, and the materials involved were assigned in ANSYS Fluent based on Table 1, with their thermal properties taken from values reported in technical literature and ANSYS databases.

Meshing of the complete system

Independent meshes were generated for the porous medium characterization and for the simulation of the complete system.

To ensure stability, a grid independent study was developed. For the square cells, shown in Table 2, a relative error of less than 0.07% is observed with 153,221 cells, similarly for the hexagonal cells with 138,943 elements.

For the complete system, shown in Table 3, with 323,732 elements, the relative error is 0.282%. These values indicate robust convergence, demonstrating that the model is highly reliable for evaluating the hybrid heating strategies proposed in this study [20].

In the partial simulations of the monolith channels, a conformal mesh was employed, as

Table 1. Relevant materials and thermal properties

Component	Main material	Thermal conductivity (W/m·K)	Function
Helical resistor	Nickel-chromium alloy (NiCr)	14.6	Direct heat source
Resistor housing	AISI 304	16.2	Radial conduction
Converter housing	AISI 304	16.2	Radial conduction
Catalyst substrate	Cordierite	1.5	Thermal Matrix
Primary exhaust pipe	AISI 304	16.2	Improve exhaust gas flow
Catalytic layer	Alumina + Pt/Pd/Rh	5	CO and HC oxidation

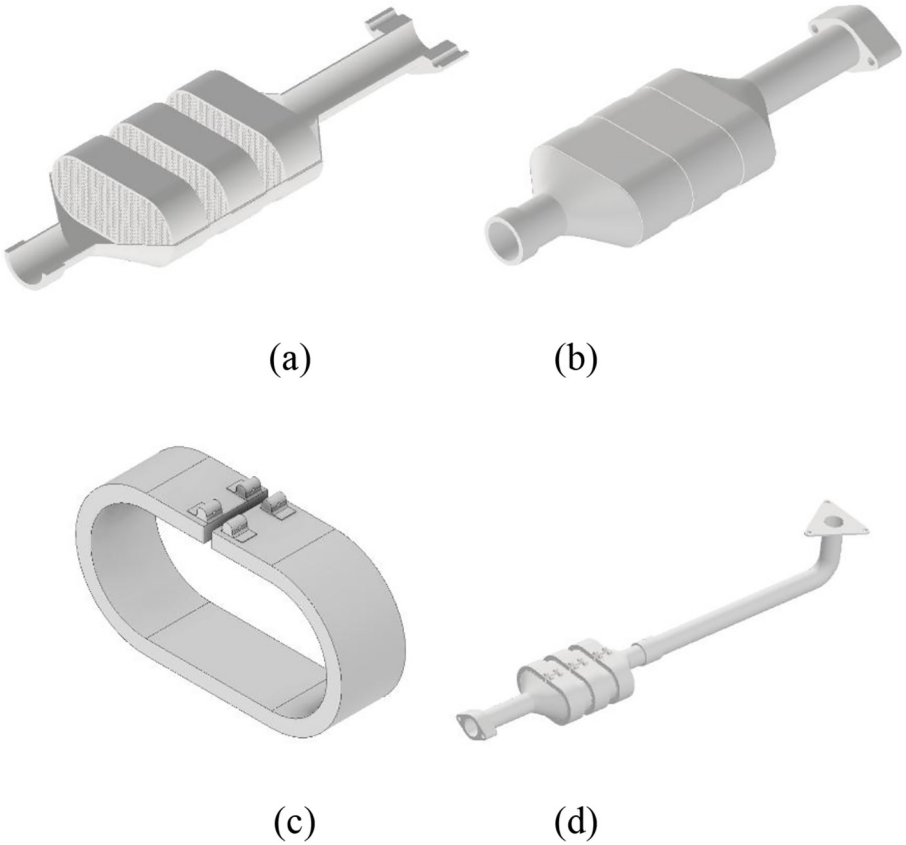

Figure 1. Designs and assemblies developed. Internal view (a), catalytic converter assembly (b), band-type heating resistor (c) and Complete system (d)

shown in Figure 2, achieving minimum orthogonal quality values greater than 0.16 for the square and hexagonal cell geometries [21].

For the simulation of the complete system (downpipe and catalytic converter), a non-conformal mesh was used, as shown in Figure 3, which allowed refinement of regions with high thermal gradients without significantly increasing computational cost. The minimum orthogonal quality achieved was 0.242, which is considered adequate for transient heat transfer simulations [21].

The mesh refinement procedure was performed by progressively reducing both the global volume element size and the surface element size within the fluid and solid domains. Additional local refinements were applied near the monolith sections, heater interfaces, and fluid-solid interaction regions to improve the resolution of thermal gradients and flow behavior. Inflation layers were incorporated adjacent to heated and wall surfaces to improve near-wall thermal boundary layer representation. The final mesh configuration predominantly consisted of unstructured tetrahedral elements with localized refinement zones and controlled element growth rates to maintain numerical stability and mesh quality during transient simulations. During the mesh independence analysis, the refinement strategy

Table 2. Mesh convergence analysis for porous medium characterization

Case	Number of elements	Max. temperature (K)	Pressure drop (Pa)	Relative error (%)
Square cells	45127	560.501	194.833	-
	72378	568.122	200.203	2.690
	98976	572.441	203.102	1.468
	125122	574.902	204.757	0.831
	153221	575.002	204.991	0.076
	185451	575.031	205.010	0.010
	225926	575.063	205.020	0.008
Hexagonal cells	40331	560.500	338.200	-
	65027	568.122	347.100	2.624
	85009	572.441	352.400	1.506
	112125	574.880	354.730	0.753
	138943	574.990	355.030	0.057
	165037	575.006	355.001	0.003
	200194	575.013	355.002	0.001

Table 3. Mesh convergence analysis for complete system

Case	Number of elements	Max. temperature (K)	Light-off time (s)	Relative error (%)
Complete system	121,347	752.807	125.407	-
	176,892	763.121	110.811	7.938
	214,563	770.274	101.292	5.665
	272,108	772.830	100.560	0.659
	323,732	773.025	100.040	0.282
	386,419	773.040	100.002	0.024
	459,271	773.073	99.999	0.006

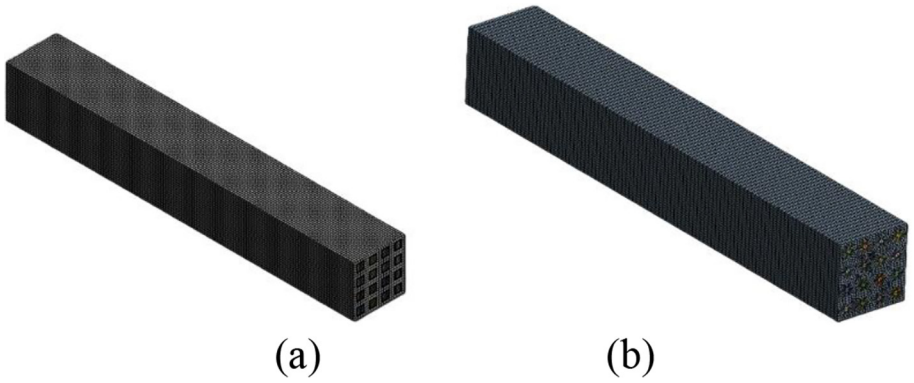

Figure 2. Mesh for porous media characterization. Square cells (a) and Hexagonal cells (b)

included modifications in minimum element size, local refinement density, and surface discretization while maintaining acceptable orthogonality and skewness values. Figure 3 illustrates the representative mesh topology and local refinement regions adopted for the simulations.

Models and assumptions

Models and assumptions

For the characterization of the porous medium, a simplified configuration was employed, using the energy model together with laminar

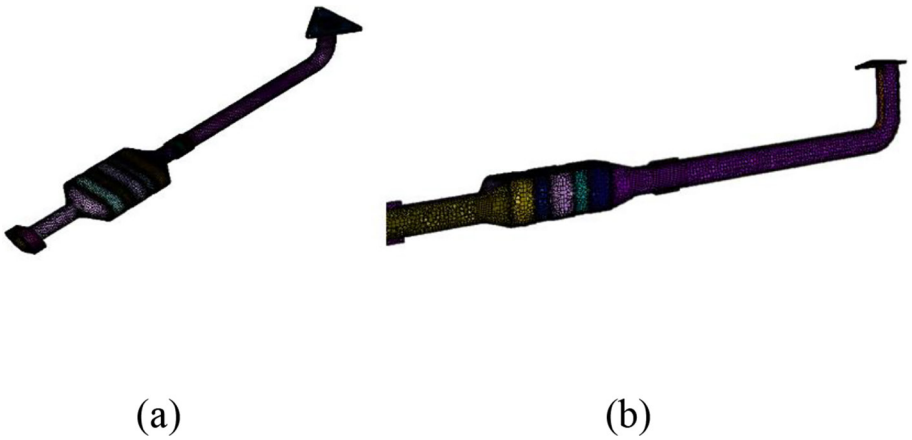

(a) (b)

Figure 3. Mesh of the complete system. Isometric view (a) and Cutaway isometric view (b)

flow and a steady-state approach, since the objective at this stage was to determine the relationship between pressure drop and flow velocity under controlled thermal conditions.

On the other hand, for the simulation of the complete system, a pressure-based solver with a transient formulation was selected to analyze heat transfer and distribution within the ceramic monolith, as well as to evaluate the light-off time. In addition, the k-omega SST turbulence model, resolved with Equation 1 and Equation 2, was used to capture turbulence in regions where the flow is neither linear nor ordered, and account for possible recirculation zones which are unique to the SST formulation to ensure model stability [21, 22]. The k-ω SST turbulence model was selected because it combines the near-wall accuracy of the standard k-ω formulation with the free-stream stability of the k-ε model, making it suitable for internal flows with adverse pressure gradients, flow separation, and localized recirculation zones. These flow characteristics are expected in the present catalytic converter configuration due to the interaction between the exhaust gases, porous monolith regions, and sudden geometric transitions between the downpipe and catalyst sections. In addition, the SST formulation has been widely applied in conjugate heat transfer and catalytic converter CFD studies, showing stable and reliable predictions for transient thermo-fluid simulations [21, 17].

$$\frac{\partial}{\partial t}(\rho k) + \frac{\partial}{\partial x_i}(\rho k u_i) = \frac{\partial}{\partial x_j}\left[\Gamma_k \frac{\partial k}{\partial x_j}\right] + G_k - Y_k \tag{1}$$

$$\frac{\partial}{\partial t}(\rho \omega) + \frac{\partial}{\partial x_i}(\rho \omega u_i) = \frac{\partial}{\partial x_j}\left[\Gamma_\omega \frac{\partial \omega}{\partial x_j}\right] + G_\omega - Y_\omega + D_\omega \tag{2}$$

The mathematical model of simulations is governed by the conservation laws of fluid dynamics. The conservation of mass Equation 3 and momentum Equation 4. are solved using a pressure-based approach with the SIMPLE algorithm and employing second-order discretization schemes, where the effect of the porous monolith is integrated as a source term Si [14, 15].

$$\frac{\partial \rho}{\partial t} + \nabla \cdot (\rho u) = 0 \tag{3}$$

$$\rho\left(\frac{\partial u}{\partial t} + u \cdot \nabla u\right) = \nabla - p + (\mu + \mu_t) \cdot \cdot \left[(\nabla u + \nabla u^T) - \frac{2}{3}\nabla \cdot uI\right] + S_i \tag{4}$$

where: *Si* is the momentum source term representing the pressure drop through the porous medium, calculated using the Darcy-Forchheimer law Equation 10.

The exhaust gases were modeled using a velocity inlet condition, considering an average temperature of 773.15 K and a velocity of 6.83 m/s. These values were selected to represent typical low-load cold-start operating conditions in light commercial vehicle exhaust systems, consistent with temperature and flow ranges reported in previous catalytic converter thermal studies [3, 17]. The use of constant inlet conditions was adopted to isolate and evaluate the thermal response of the proposed heating strategies under controlled and repeatable transient conditions.

The simulations were carried out with a time step of 0.5 seconds, selected as a compromise between temporal resolution, numerical stability, and computational cost for the transient cold-start simulations performed in this study. For each transient time step, the numerical solution was iterated until achieving residual convergence levels below 10^{-4} for continuity and momentum equations and below 10^{-6} for the energy equation. In addition, numerical convergence was verified through the stabilization of global thermal variables together with monitoring of global mass and energy balances [23]. Due to the computational cost associated with the complete conjugate transient simulations, a formal time-step independence analysis and detailed y^+ assessment were not included in the present study and are recommended for future numerical investigations.

Heat transfer

For heat transfer, the energy model, which accounts for energy transport due to advection, conduction, and viscous dissipation, was activated. This model is governed by energy equation shown in Equation 5 [22].

$$\frac{\partial}{\partial t}\left(\rho\left(e+\frac{v^2}{2}\right)\right)+\nabla\cdot\left(\rho\vec{v}\left(h+\frac{v^2}{2}\right)\right)= =\left(k_{eff}\nabla T-\sum_j h_j\vec{J}_J+\underline{\tau_{eff}}\cdot\vec{v}\right)+S_h \quad (5)$$

where: *Sh* accounts for the heat generated by the electrical resistances (EHC and band heaters).

Heat exchange with the ambient was modeled using Newton's Law of Cooling equation shown in Equation 6, with convection coefficients of 12 W/m²K and 15 W/m²K for the catalytic converter casing and the primary exhaust pipe, respectively. These coefficients are within the range commonly reported for natural and mixed convection heat transfer in external automotive exhaust components under low-speed operating conditions [21, 25].

$$q = H\cdot(T_{wall}-T_{amb}) \quad (6)$$

For solids heat transfer within solid regions the energy equation is simplified in Equation 7.

$$\frac{\partial}{\partial t}(\rho h)+\nabla\cdot(\vec{v}\rho h)=\nabla\cdot(k\nabla T)+S_h \quad (7)$$

The thermal interaction between the fluid and solid domains was configured using conjugate heat transfer (CHT) with coupled wall interfaces, ensuring the continuity of heat flux at the boundaries [23].

$$k_f\left(\frac{\partial T_f}{\partial n}\right)_{wall}=k_s\left(\frac{\partial T_s}{\partial n}\right)_{wall} \quad (8)$$

Porous medium characterization (ceramic monoliths)

The ceramic monolith can be represented as an equivalent porous medium, since direct modeling of the monolith by considering each individual cell would involve a high computational cost [29]. Flow through the porous medium is described by the Darcy-Forchheimer equation shown in Equation 9 and Equation 10, which introduces viscous and inertial resistance terms into the momentum equations [14, 15].

$$S_i=-\left(K\mu v+\frac{C_2}{2}\rho v^2\right) \quad (9)$$

$$\frac{\Delta P}{L}=-S_i=-\left(K\mu v+\frac{C_2}{2}\rho v^2\right) \quad (10)$$

where: ΔP is the pressure drop between the inlet and outlet of the porous medium [24], [25, 26].

The coefficients were determined through a prior CFD characterization of the ceramic monolith, based on the simulation of a representative section of the internal channels, as shown in Figure 4. The simulations were performed using air flow at a constant temperature of 575 K and different inlet velocities ranging from 2 to 20 m/s. The relationship between Δp and air velocity was obtained through quadratic regression using a Python-developed script, assuming that air has a density of 0.615 kg/ms³ and a dynamic viscosity of $(2.91\cdot10^{-5}$ kg)/ms [25, 26]. Additionally, the porosity of the monolith was calculated from the three-dimensional geometric model [25]. The monolith was defined as an anisotropic porous medium by applying the viscous and inertial resistance coefficients in the axial flow direction. To represent the transverse impermeability of the monolith, significantly higher resistances were assigned in other directions. Likewise, local thermal equilibrium between the gaseous phase and the cordierite solid matrix was assumed,

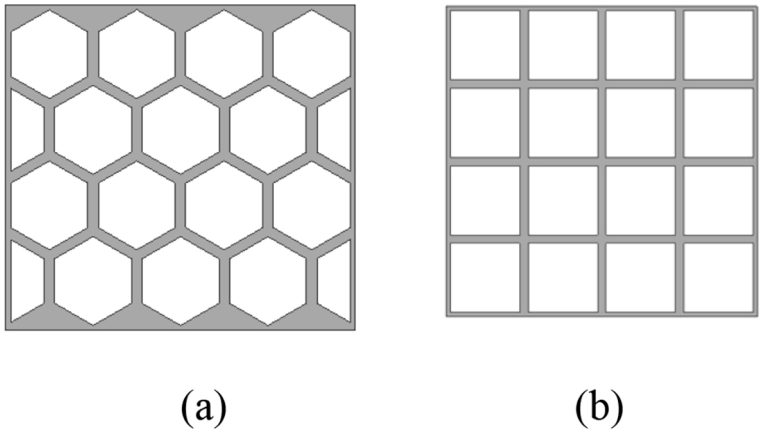

Figure 4. Extracted parts for porous media characterization. Hexagonal cells (a) and Square cells (b)

considering a single representative temperature within the porous domain.

Modeling of heat sources (band-type heaters and EHC)

Band-type heaters were modeled as a surface heat source, defined in ANSYS Fluent in terms of heat flux, this value is obtained by dividing the total power of the heating element by the sum of the areas of all faces and multiplying it by an efficiency factor, as shown in the Equation 11.

$$E = \frac{P}{a} \cdot \eta = \frac{500\,W}{0.945\,m^2} \cdot 0.8 = 43386.16 \frac{W}{m^2} \quad (11)$$

An efficiency factor of η = 0.8 was adopted to account for thermal losses associated with conduction through supporting structures and heat dissipation to the surroundings. Similar efficiency assumptions have been reported in electrically assisted heating studies for automotive thermal systems [10, 11].

Where E is the value to be specified in ANSYS, P is the power of the heating element, A is the total area of the external faces of the heater, and η is the efficiency. For the EHC case, heating was modeled through a volumetric heat source applied within the porous domain of the ceramic monolith. The volumetric heat generation rate was established based on power values reported in the literature for EHC systems, ensuring thermal conditions that are representative and comparable to real applications. In addition, an upper thermal threshold was implemented as a numerical stabilization criterion to prevent unrealistically high localized temperatures in the heating elements and solid regions during transient simulations. The selected limits (900 K for the solid domain and 1023.15 K for external heater surfaces) were based on temperature ranges commonly associated with catalyst material durability and electrically heated metallic components reported in previous studies [6, 7]. The imposed threshold acts only under extreme localized overheating conditions and did not significantly affect the overall thermal trends, light-off behavior, or comparative performance between heating configurations [27].

Chemical kinetics model

The chemical kinetics model implemented in this study was intentionally decoupled from the CFD simulation in order to reduce computational complexity and focus primarily on the transient thermal activation behavior of the catalyst during cold-start conditions. Therefore, the pollutant conversion analysis was performed as a post-processing stage using temperature histories obtained from the CFD simulations. This simplified approach assumes that the thermal field predicted by the CFD model is the dominant factor governing catalyst activation and pollutant conversion trends. However, it does not fully account for the simultaneous interaction between flow dynamics, species transport, and heterogeneous catalytic reactions inside the monolith. Consequently, the obtained emission values should be interpreted as an approximate estimation of catalyst performance under transient thermal conditions. Despite these limitations, similar decoupled approaches based on Arrhenius-type formulations shown in Equation 12 have been previously employed in preliminary catalytic converter performance analyses and thermal management studies [13, 17].

$$k_i(T) = A_i \cdot e^{-\frac{E_{ai}}{RT}} \quad (12)$$

It is important to note that the specific values for Ai and Eai used in this study were extracted from [13, 14] ensuring that the kinetic model accurately reflects the behavior of CO and NO oxidation under typical automotive exhaust conditions. The instantaneous conversion efficiency (η) is determined as a function of the Equation 14. Subsequently the instantaneous mass flow emissions were calculated considering the raw exhaust gas mass flow (m_{gas}) and the initial pollutant concentration (Ci) which was extracted from [28], [29]. Equation 13.

$$\eta\big(T(t)\big) = \left(1 - e^{-k_i(T)\cdot t_{res}}\right) \cdot 0.9 \quad (13)$$

$$\dot{m}_{out}(t) = \dot{m}_{gas} \cdot C_i \cdot \left[1 - \eta\big(T(t)\big)\right] \quad (14)$$

where: t_{res} was calculated with Equation 15.

$$t_{res} = \frac{L}{v_{in}} \quad (15)$$

Finally, the total mass emitted (M_{total}) during the transient cold-start period was obtained through a discrete numerical integration shown in Equation 16 [13].

$$M_{total} = \sum_{t=0}^{t_{final}} (\dot{m}_{out}(t) \cdot \Delta t) \quad (16)$$

Integration with WLTP cycle and Euro 7 standards

To standardize the emission results, the accumulated pollutant mass obtained from the post-processing analysis was extrapolated using a simplified WLTP-based approach considering a cycle duration of 30 minutes and an average vehicle velocity of 46.5 km/h, resulting in an equivalent traveled distance of approximately 23.25 km [11, 30]. The WLTP cycle was not reproduced dynamically in the CFD simulation. Instead, constant representative operating conditions were adopted to isolate and compare the thermal response of the different heating strategies under controlled cold-start conditions. Consequently, the present approach does not capture transient variations in engine load, exhaust mass flow rate, or temperature fluctuations characteristic of real driving cycles. Therefore, the obtained emission values should be interpreted as comparative estimations intended for evaluating the relative effectiveness of the proposed thermal management strategies rather than exact real-world emission predictions. Future work should incorporate transient driving-cycle boundary conditions and fully coupled engine-exhaust simulations.

Model verification, numerical uncertainty and limitations

To ensure numerical reliability, a mesh independence analysis was conducted for both the porous media characterization and the complete transient thermal model, as presented in Tables 2 and 3. The selected meshes exhibited relative errors below 0.3%, indicating stable numerical behavior, limited discretization sensitivity, and grid-independent solutions.

In addition, transient simulations were performed using a time step of 0.5 s, which provided stable convergence behavior for the thermal variables and light-off predictions. Numerical convergence was verified through monitoring of continuity, momentum, and energy residuals together with global mass and energy balances.

Due to the conceptual nature of the proposed hybrid electrically assisted catalyst configuration and the absence of equivalent experimental datasets in the literature, direct experimental validation was not possible. Therefore, the verification approach adopted in this study was based on: (i) numerical convergence verification, (ii) mesh independence analysis, and (iii) qualitative benchmarking against previously published CFD and experimental studies on catalyst light-off and thermal behavior.

The obtained trends regarding pressure drop variation with flow velocity, transient temperature evolution inside the monolith, and reduction of catalyst light-off time under electrically assisted heating are qualitatively consistent with previously published CFD and experimental studies reported by Hayes et al. [25], Benjamin and Roberts [31], and Jeong and Kim [32].

Nevertheless, the present study is subject to several sources of uncertainty, including the simplified porous-medium representation of the monolith, constant inlet boundary conditions, simplified convective heat transfer coefficients, and the decoupled chemical kinetics model employed during post-processing. Therefore, the obtained results should be interpreted as comparative numerical estimations intended to evaluate relative thermal performance trends between the proposed heating strategies.

RESULTS

Porous medium characterization

The CFD simulations performed for the square and hexagonal monolith geometries produced the pressure drop values presented in Table 4. Table 4 shows that the pressure drop increases nonlinearly with increasing inlet velocity for both geometries, indicating the combined influence of viscous and inertial effects inside the monolith channels. For the square-cell geometry, the pressure drop increased from 79.35 Pa at 2 m/s to 957.84 Pa at 20 m/s. Similarly, for the hexagonal-cell configuration, the pressure drop increased from 139.73 Pa to 1546.56 Pa over the same velocity range. The quadratic regression curves obtained from the pressure drop analysis exhibited coefficients of determination greater than 0.999 for both geometries. Based on these correlations, the viscous and inertial resistance coefficients required for the porous-medium model were determined. In addition, the porosity values obtained from the three-dimensional geometric characterization confirmed that the square-cell monolith exhibited lower hydraulic resistance compared to the hexagonal configuration. Figures 5(a) and 5(b) present the pressure drop evolution as a function of inlet velocity for the square and hexagonal geometries, respectively.

Table 4. Pressure drop on the square and hexagonal monolith geometries for velocities from 2 m/s to 20 m/s

Square cells		Hexagonal cells	
Velocity (m/s)	Pressure drop (Pa)	Velocity (m/s)	Pressure drop (Pa)
2	79.3598	2	139.7324
5	205.386	5	355.7519
10	433.6867	10	732.2971
15	684.5204	15	1129.166
20	957.845	20	1546.56

Comparison of square and hexagonal cells

Figures 6 and 7 present the temperature contour maps obtained for the systems with square and hexagonal monolith cells, respectively. In both cases, heat transfer from the exhaust gases to the ceramic monolith promoted progressive thermal activation along the catalyst length. For the square-cell configuration, higher peak temperatures were observed in the first monolith region, while the hexagonal-cell geometry exhibited a more uniform temperature distribution throughout the catalytic converter. It is important to note that all contour plots presented in Figures 6 and 7 were generated using identical temperature scale ranges in order to ensure consistent qualitative comparison between the evaluated heating configurations from 293 K to 873 K.

Figure 8 shows the transient thermal evolution of the three monolith sections for both geometries. The square-cell configuration reached the light-off temperature faster in all monolith sections. The corresponding light-off times are summarized in Table 5. The square-cell geometry reached the light-off condition at approximately 100 s, 250 s, and 390 s for the first, second, and third monoliths, respectively. In contrast, the hexagonal-cell configuration required approximately 200 s, 370 s, and 490 s. The thermal uniformity analysis using the Area Uniformity Index yielded average values of 0.96605 for the square-cell configuration and 0.97858 for the hexagonal-cell geometry.

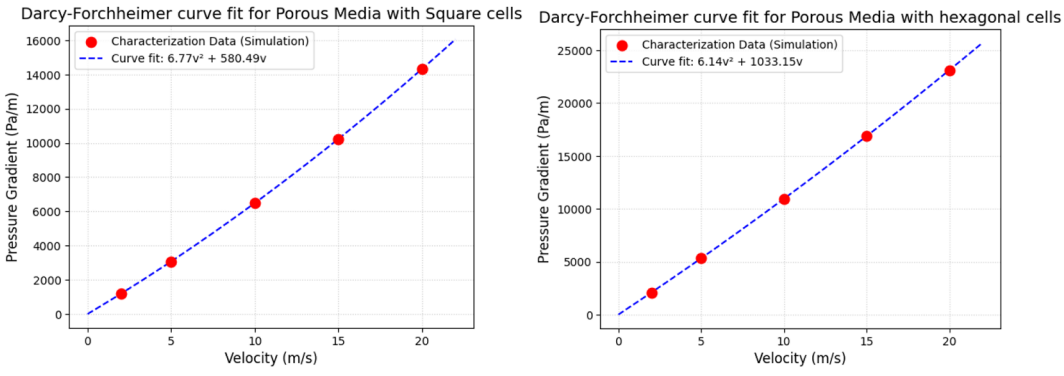

(a) (b)

Figure 5. Pressure drop as a function of inlet velocity for square-cell monoliths (a) and hexagonal-cell monoliths (b)

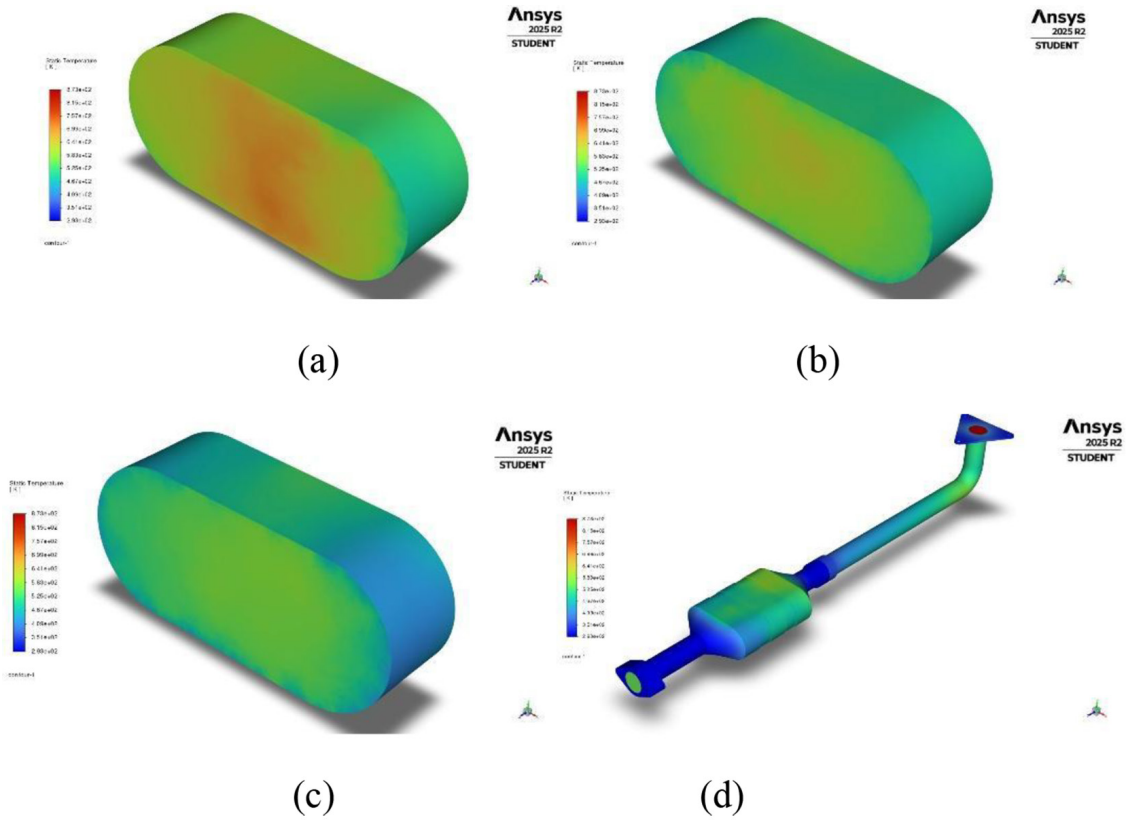

Figure 6. Temperature contour maps for systems with square cells. Inlet monolith (a), Intermediate monolith (b), Outlet monolith (c) and Complete system (d)

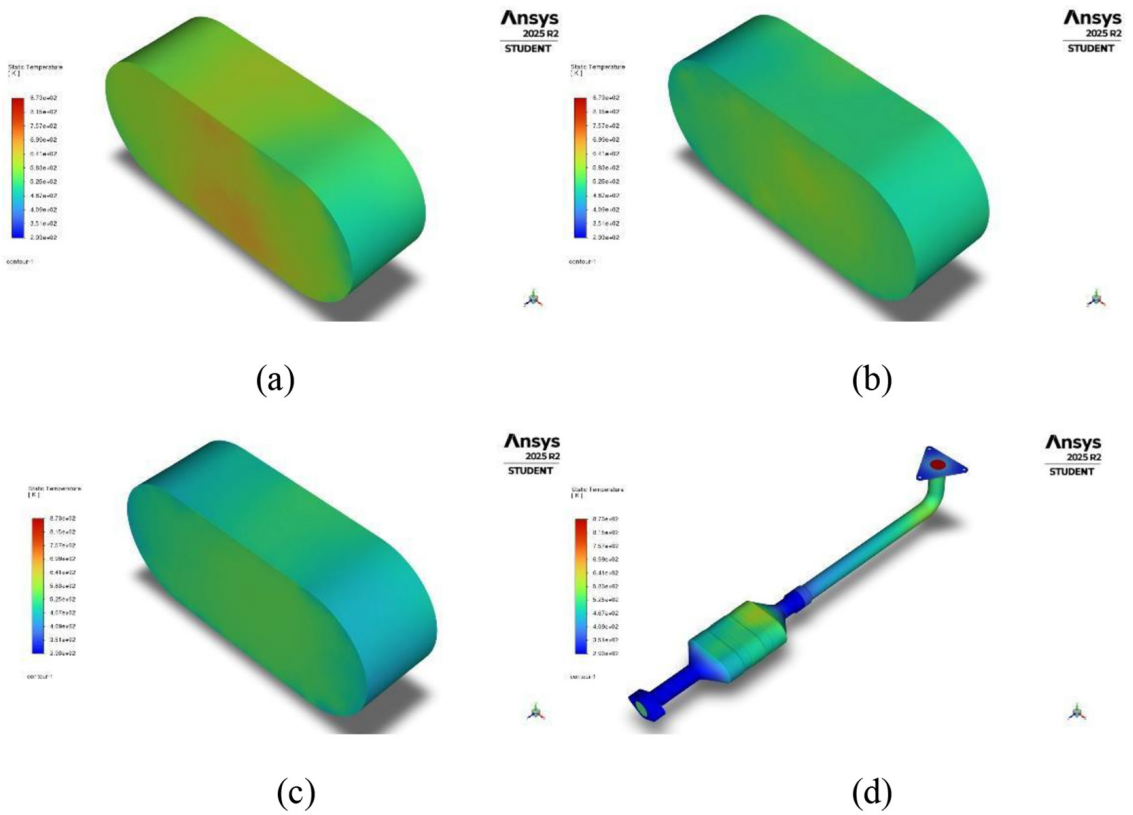

Figure 7. Temperature contour maps for systems with hexagonal cells. Inlet monolith (a), Intermediate monolith (b), Outlet monolith (c) and Complete system (d)

Table 5. Time to reach light-off temperature

Cell	Square cells	Hexagonal cells
1st cell	100 s	200 s
2nd cell	250 s	370 s
3rd cell	390 s	490 s

Comparative analysis of electrical heating strategies for the catalyst

The thermal performance of the catalyst was evaluated under three electrically assisted heating strategies: electrically heated catalyst (EHC), band-type heating resistances, and hybrid heating. Figure 9 presents the transient temperature evolution for the three monolith sections under each heating configuration. The incorporation of electrical heating significantly accelerated the catalyst activation process compared to the baseline configuration without electrical assistance. The light-off times obtained for each configuration are summarized in Table 6. The EHC system reached the light-off condition for the third monolith in approximately 118 s,

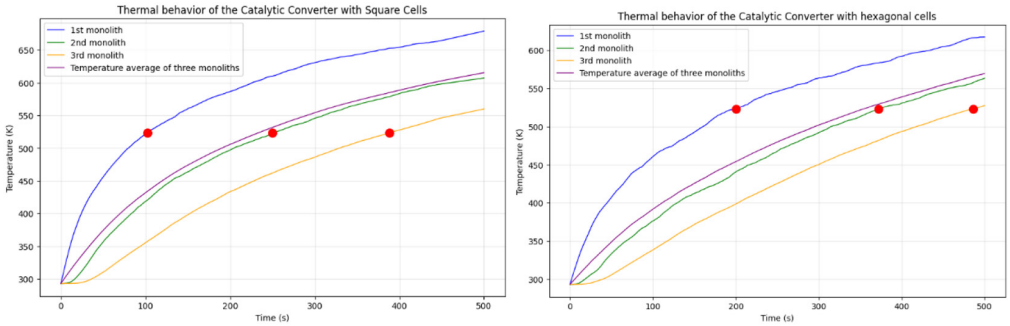

(a) (b)

Figure 8. Temperature of the three ceramic monoliths and their average. Square cells (a) and Hexagonal cells (b)

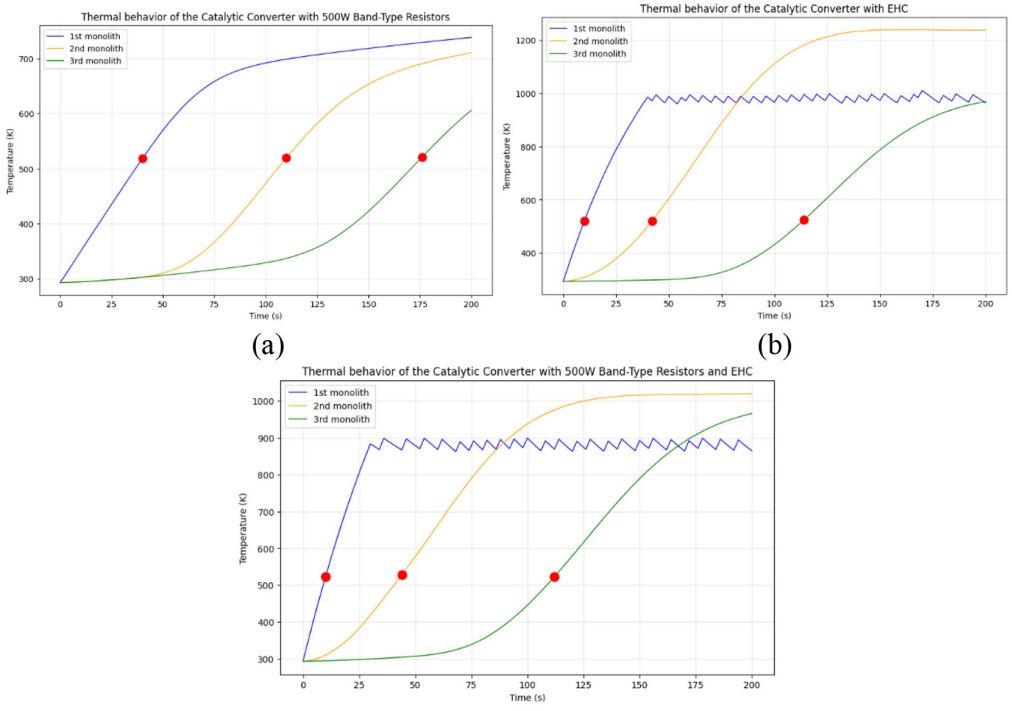

(a) (b)

(c)

Figure 9. Temperature of the three ceramic monoliths and their average with electrical heating. band-type resistances (a), Internal EHC (b) and Hybrid configuration (c)

Table 6. Time to reach the light-off temperature and thermal uniformity indices

Cell	EHC	Band-type resistance	Hybrid
1st cell	10 s	10 s	10 s
2nd cell	46 s	110 s	37 s
3rd cell	118 s	176 s	112 s

while the band-type heating system required 176 s. The hybrid configuration achieved the shortest activation time, reaching light-off in approximately 112 s.

Figures 10–12 present the temperature contour distributions obtained for the three heating configurations. The EHC configuration produced rapid heating in the first monolith regions but generated pronounced localized thermal gradients and peak temperatures approaching 1000 °C in localized regions. In contrast, the band-type heating configuration produced lower thermal gradients and a more gradual thermal response. The hybrid configuration promoted a more homogeneous temperature distribution along the catalyst length while simultaneously reducing localized thermal peaks. Compared with the baseline case, the hybrid heating strategy reduced the activation time of the third monolith from approximately 390 s to 112 s.

The thermal behavior predicted by the present CFD model is consistent with trends reported in previous studies on catalytic converter warm-up and light-off performance. Hayes et al. [25] reported that increased thermal uniformity and optimized monolith configurations contribute to faster catalyst activation and improved light-off behavior. Similarly, Benjamin and Roberts [31] observed that porous-medium CFD approaches are capable of reproducing transient temperature evolution and catalyst warm-up trends with reasonable agreement against experimental measurements. In addition, Jeong and Kim [32] demonstrated that flow distribution and thermal gradients strongly influence transient light-off performance, which agrees with the temperature distributions obtained in the present work.

Chemical kinetics results and comparative emission analysis

The post-processing chemical kinetics analysis demonstrated that electrically assisted heating significantly improved the transient catalytic conversion behavior during cold-start operation. The hybrid configuration exhibited the best overall emission reduction performance among the evaluated configurations. Compared with the baseline case, the hybrid strategy reduced NOx

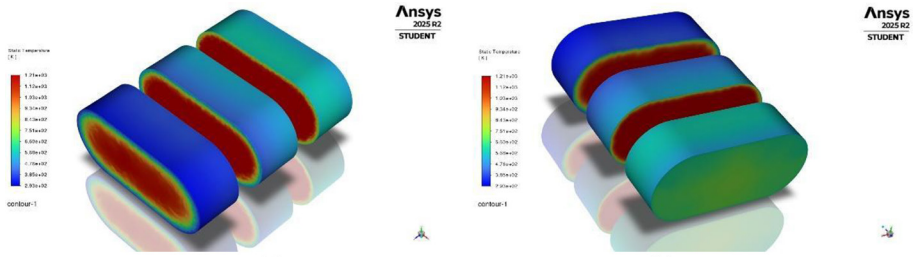

(a) (b)

Figure 10. Temperature contour map for the three monoliths heated by electrically heated catalyst. Front isometric view (a) and Rear isometric view (b)

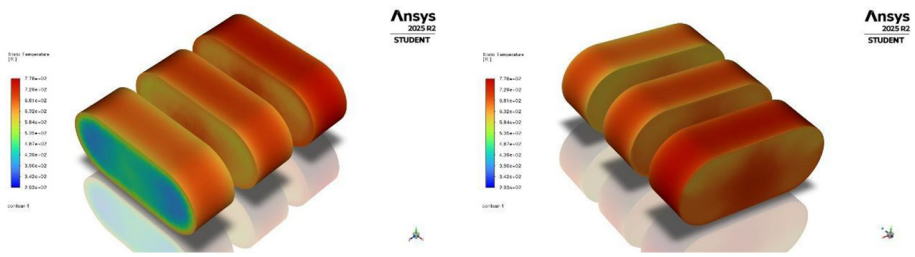

(a) (b)

Figure 11. Temperature contour map for the three monoliths heated by band-type resistances. Front isometric view (a) and Rear isometric view (b)

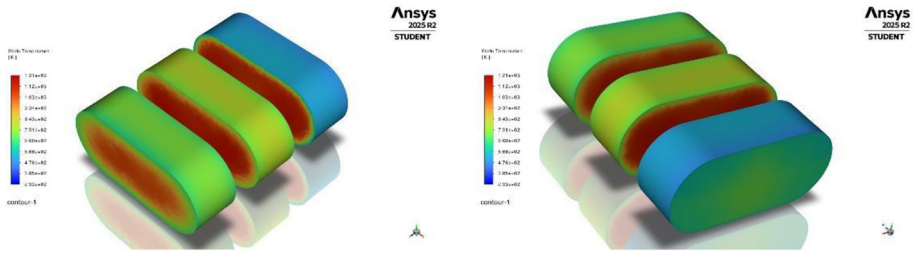

(a) (b)

Figure 12. Temperature contour map for the three monoliths heated by the hybrid configuration. Front isometric view (a) and Rear isometric view (b)

emissions by 87.12%, CO emissions by 95.41%, and HC emissions by 45.46%. The extrapolated WLTP-based analysis yielded a final NOx emission value of 47.47 mg/km for the hybrid configuration, remaining below the Euro 7 reference limit of 60 mg/km [33].

DISCUSSION

Porous medium characterization

The nonlinear increase in pressure drop observed in Figure 5 confirms that both viscous and inertial flow effects contribute to the hydraulic behavior of the ceramic monoliths. The higher pressure losses obtained for the hexagonal geometry are associated with increased flow resistance generated by the internal channel configuration. The excellent agreement obtained through quadratic regression ($R^2 > 0.999$) supports the suitability of representing the monolith as an equivalent porous medium. Similar pressure-drop behavior and porous-medium representations have been reported in previous catalytic converter CFD studies by Hayes et al. and Kovacev et al. The lower hydraulic resistance observed in the square-cell configuration contributes to improved axial heat transport through the monolith, which partially explains the faster thermal activation observed in subsequent transient simulations.

Discussion of square and hexagonal cell performance

The thermal distributions shown in Figures 6–8 indicate that the internal geometry of the monolith strongly influences both thermal uniformity and catalyst activation time. Although the hexagonal-cell geometry produced slightly more homogeneous temperature fields, the square-cell configuration achieved significantly faster light-off times. According to Table 5, the third monolith reached activation approximately 100 s earlier than the hexagonal configuration. This behavior is mainly associated with the lower hydraulic resistance and enhanced axial heat transfer obtained for the square-cell geometry, which facilitated faster propagation of thermal energy through the catalyst. The obtained thermal trends are consistent with previous studies reporting that monolith channel geometry directly affects flow distribution, heat transfer behavior, and catalyst warm-up dynamics. Considering that the difference in thermal uniformity between both geometries was relatively small, while the difference in activation time was substantial, the square-cell configuration was selected for the electrically assisted heating analysis.

Discussion of electrical heating strategies

The obtained results demonstrate that electrically assisted heating significantly accelerates catalyst activation during cold-start operation. The EHC configuration generated the fastest localized heating near the inlet monoliths due to direct volumetric heat generation inside the porous medium. However, Figures 10(a) and 10(b) reveal the formation of pronounced localized thermal gradients and thermal peaks approaching critical temperatures for catalyst durability. In contrast, the band-type heating strategy produced lower thermal gradients and improved radial heat distribution but exhibited slower activation times because heat transfer occurred primarily through external conduction. The hybrid configuration combined the advantages of both approaches by simultaneously promoting rapid thermal activation and improved thermal uniformity. As shown in Figure 12,

the hybrid strategy distributed heat more uniformly across the catalyst length while reducing localized overheating. According to Table 6, the hybrid system reduced the light-off time of the third monolith from approximately 390 s in the baseline configuration to 112 s, corresponding to a reduction of approximately 71.3%. These results indicate that combining internal and external heating mechanisms can improve transient thermal management while limiting excessive thermal stresses inside the monolith. The obtained thermal behavior is consistent with previous investigations on electrically heated catalysts, where rapid catalyst activation was achieved at the expense of increased thermal gradients in purely internal heating systems.

Discussion of emission reduction performance

The reduction in light-off time obtained through electrically assisted heating directly improved the transient pollutant conversion efficiency during cold-start operation. The hybrid configuration achieved the lowest estimated NOx, CO, and HC emissions because the catalyst reached the activation temperature significantly earlier than the baseline case. The predicted NOx emission level of 47.47 mg/km remained below the Euro 7 reference limit considered in this study. However, it should be noted that the emission analysis was based on a simplified post-processing kinetics model and simplified WLTP extrapolation. Therefore, the obtained emission values should be interpreted as comparative performance estimations rather than exact real-world emission predictions. Nevertheless, the obtained results demonstrate the potential of hybrid electrically assisted heating strategies for improving cold-start catalyst activation and reducing transient pollutant emissions in automotive exhaust systems.

CONCLUSIONS

The present study investigated the transient thermal behavior and cold-start emission reduction potential of electrically assisted heating strategies for automotive catalytic converters using a CFD-based approach combined with simplified post-processing chemical kinetics analysis. The numerical characterization of the ceramic monolith demonstrated that the internal channel geometry significantly influences both hydraulic resistance and catalyst warm-up behavior. Although the hexagonal configuration exhibited slightly improved thermal uniformity, the square-cell geometry provided faster thermal activation and was therefore selected for the electrically assisted heating analysis. Among the evaluated heating configurations, the hybrid electrically assisted strategy demonstrated the most favorable balance between rapid catalyst activation and thermal distribution uniformity. The combined use of internal and external heating mechanisms reduced catalyst light-off time and improved the predicted transient pollutant conversion performance during cold-start operation. The obtained results indicate that hybrid electrically assisted catalyst systems have significant potential for improving thermal management and reducing cold-start emissions under future low-emission regulatory scenarios. In particular, the predicted NO_x emissions obtained through the simplified WLTP-based extrapolation remained below the Euro 7 reference limit considered in this study. Nevertheless, the present work is subject to several limitations associated with the simplified porous-medium representation, constant operating conditions, and the decoupled chemical kinetics approach adopted during post-processing. Therefore, the obtained emission values should be interpreted as comparative numerical estimations rather than exact real-world predictions. Future work should focus on implementing fully coupled reactive CFD simulations, transient driving-cycle boundary conditions, and experimental validation using a full-scale prototype under real operating conditions in order to assess long-term thermal durability and catalyst performance.

Acknowledgements

We thank the Universidad Nacional de San Agustín de Arequipa for their support and knowledge.

REFERENCES

1. Kritsanaviparkporn E., Baena-Moreno F.M., Reina T.R. Catalytic converters for vehicle exhaust: fundamental aspects and technology overview for newcomers to the field. Chemistry 2021;3:630–46.

https://doi.org/10.3390/chemistry3020044

2. Li Y., Hu J., Li J., Xu H., Wu Y., Cai Z., et al. Experimental study on electrically heated catalyst coupling strategies for ultra-low emissions and energy-efficient thermal management in diesel engines. Applied Thermal Engineering 2025;280:128450. https://doi.org/10.1016/j.applthermaleng.2025.128450
3. Steiner T., Neurauter D., Moewius P., Pfeifer C., Schallhart V., Moeltner L. Heat-up performance of catalyst carriers—a parameter study and thermodynamic analysis. Energies 2021;14:964. https://doi.org/10.3390/en14040964
4. Robles-Lorite L., Dorado-Vicente R., Torres-Jiménez E., Bombek G., Lešnik L. Recent advances in the development of automotive catalytic converters: A systematic review. Energies 2023;16:6425. https://doi.org/10.3390/en16186425
5. Tronconi E., Groppi G., Visconti C.G.. Structured catalysts for non-adiabatic applications. Current Opinion in Chemical Engineering 2014;5:55–67. https://doi.org/10.1016/j.coche.2014.04.003
6. Choi I.-H., Seo M.W., Ra H.W., Lee K.-Y., Hwang K-R. Advanced approach for catalytic decomposition of tar: Electrically heated catalyst system. Chemical Engineering and Processing - Process Intensification 2021;165:108407. https://doi.org/10.1016/j.cep.2021.108407
7. Kleschew D., Sentko M., Nieken U. Electrically heated multilayer ceramic composite tubes for high-temperature endothermic reactions. Chemie Ingenieur Technik 2025;97:608–17. https://doi.org/10.1002/cite.202500005
8. Duan L., Tan P., Liu J., Liu Y., Chen Y., Lou D., et al. Emission characteristics of a diesel engine with an electrically heated catalyst under cold start conditions. Journal of Cleaner Production 2022;380:134965. https://doi.org/10.1016/j.jclepro.2022.134965
9. Canè S., Brunelli L., Gallian S., Perazzo A., Brusa A., Cavina N. Performance assessment of a predictive pre-heating strategy for a hybrid electric vehicle equipped with an electrically heated catalyst. Applied Thermal Engineering 2023;219:119341. https://doi.org/10.1016/j.applthermaleng.2022.119341
10. Ning J., Yan F. Temperature control of electrically heated catalyst for cold-start emission improvement. IFAC-PapersOnLine 2016;49:14–9. https://doi.org/10.1016/j.ifacol.2016.08.003
11. Marchenkova M.A., Gadzhiev J.K., Guda A.A., Soldatov A.V., Chapek S.V. Three-dimensionally printed catalytic structures. Journal of Manufacturing and Materials Processing 2025;9:372. https://doi.org/10.3390/jmmp9110372
12. Cornejo I., Nikrityuk P., Hayes R.E. The influence of channel geometry on the pressure drop in automotive catalytic converters: Model development and validation. Chemical Engineering Science 2020;212:115317. https://doi.org/10.1016/j.ces.2019.115317
13. Hua Q., Shen B. Simulation of selective catalytic reduction of NO and oxidation of CO and C7H8 over V_2O_5-TiO_2 catalyst. Journal of the Energy Institute 2025;119:101956. https://doi.org/10.1016/j.joei.2024.101956
14. Rodriguez J.F., Cheng W.K. Analysis of NOx emissions during crank-start and cold fast-idle in a GDI engine. SAE Int J Engines 2017;10:646–55. https://doi.org/10.4271/2017-01-0796
15. Tan Y., Kou C., Ning D., E. J., Feng C. Effects of the structure parameters on methane emission control of an adsorptive three-way catalytic converter during cold start of the heavy-duty natural gas engines. Energy 2025;317:134654. https://doi.org/10.1016/j.energy.2025.134654
16. Euro 4x4 Car Parts: Exhaust - Catalytic converter TOYOTA Hilux 7 Vigo 2005->2015 [Internet]. Euro4x4parts. [Cited in May 2026]. Available: https://www.euro4x4parts.com/en/parts/catalog-specific/toyota-hilux-7-vigo-2005-2015-2-5-d4d-kun25-4x4-diesel-2005-2011/engine/exhaust/catalytic-converter
17. Toyota Motor Europe - Toyota Service Information - Technical Portal [Internet]. Toyota Service Information - Repair Manual & New Car Features [Cited in May 2026]. Available: https://www.toyota-tech.eu
18. Zoppas Industries - High-Performance Band Heaters: Technical Specifications and Material Properties [Internet]. Zoppas Industries - Heating Element Technologies [Cited in May 2026]. Available: https://zoppasindustries.com/en/band-heaters/
19. McMaster-Carr - Band Heaters for Extrusion and Industrial Applications - Dimensional Data [Internet] Available: https://www.mcmaster.com/products/band-heaters/
20. Vivarelli G., Qin N., Shahpar S. A review of mesh adaptation technology applied to computational fluid dynamics. Fluids 2025;10:129. https://doi.org/10.3390/fluids10050129
21. Myronov A., Ilchenko M., Ponomarenko Y., Gorbunov K., Bykanov S., Ponomarenko H., et al. Development of elements of an informational-and-mathematical model of hydrodynamic processes in a ceramic catalytic converter for developing an enterprise computer simulation model. TAPR 2024;6:12–6. https://doi.org/10.15587/2706-5448.2024.319177
22. Ansys Inc. - Ansys Fluent Theory Guide, Release 2024 R2 [Internet] Ansys, Inc. Available: https://ansyshelp.ansys.com/public/account/secured?returnurl=//Views/Secured/corp/v242/en/flu_th/flu_th.html

23. Lewis M.T., Hickey J.P. Conjugate heat transfer in high-speed external flows: A review. Journal of Thermophysics and Heat Transfer 2023;37:697–712. https://doi.org/10.2514/1.t6763
24. Wang K., Wang G., Chen H., Zhu L. Estimating thermal boundary conditions of boiler membrane water-wall using decentralized fuzzy inference with sensitivity weighting. Applied Thermal Engineering 2014;66:309–17. https://doi.org/10.1016/j.applthermaleng.2014.02.020
25. Hayes R.E., Fadic A., Mmbaga J., Najafi A. CFD modelling of the automotive catalytic converter. Catalysis Today 2012;188:94–105. https://doi.org/10.1016/j.cattod.2012.03.015
26. Chaparro-Garnica C.Y., Bailón-García E., Davó-Quiñonero A., Lozano-Castelló D., Bueno-López A. Sponge-like carbon monoliths: Porosity control of 3D-printed carbon supports and its influence on the catalytic performance. Chemical Engineering Journal 2022;432:134218. https://doi.org/10.1016/j.cej.2021.134218
27. Bhaskar K., Sassykova L.R., Prabhahar M., Percis E.S., Nalini A., Jenish T., et al. Resistance heated catalytic converter (RHCC) with copper oxide catalyst for reducing HC/CO emission from automobile. Materials Today: Proceedings 2021;45:5868–72. https://doi.org/10.1016/j.matpr.2020.08.330
28. Šarkan B., Loman M., Synák F., Skrúcaný T., Hanzl J. Emissions production by exhaust gases of a road vehicle's starting depending on a road gradient. Sensors 2022;22:9896. https://doi.org/10.3390/s22249896
29. Khoa N.X., Lim O. A review of the external and internal residual exhaust gas in the internal combustion engine. Energies 2022;15:1208. https://doi.org/10.3390/en15031208
30. Barbier A., Salavert J.M., Palau C.E., Guardiola C. Analysis of the Euro 7 on-board emissions monitoring concept with real-driving data. Transportation Research Part D: Transport and Environment 2024;127:104062. https://doi.org/10.1016/j.trd.2024.104062
31. Benjamin S.F., Roberts C.A. Automotive catalyst warm-up to light-off by pulsating engine exhaust. International Journal of Engine Research 2004;5:125–47. https://doi.org/10.1243/146808704773564541
32. Kuta K., Nadimi E., Przybyła G., Żmudka Z., Adamczyk W. Ammonia CI engine aftertreatment systems design and flow simulation. Combustion Engines 2021. https://doi.org/10.19206/ce-143158
33. Mulholland E., Miller J., Bernard Y., Lee K., Rodríguez F. The role of NOx emission reductions in Euro 7/VII vehicle emission standards to reduce adverse health impacts in the EU27 through 2050. Transportation Engineering 2022;9:100133. https://doi.org/10.1016/j.treng.2022.100133